Simulations of Atmospheric Rivers, Their Variability, and Response to Global Warming Using GFDL's New High-Resolution General Circulation Model

MING ZHAO

Geophysical Fluid Dynamics Laboratory, Princeton, New Jersey

(Manuscript received 6 April 2020, in final form 19 July 2020)

ABSTRACT: A 50-km-resolution GFDL AM4 well captures many aspects of observed atmospheric river (AR) characteristics including the probability density functions of AR length, width, length–width ratio, geographical location, and the magnitude and direction of AR mean vertically integrated vapor transport (IVT), with the model typically producing stronger and narrower ARs than the ERA-Interim results. Despite significant regional biases, the model well reproduces the observed spatial distribution of AR frequency and AR variability in response to large-scale circulation patterns such as El Niño–Southern Oscillation (ENSO), the Northern and Southern Hemisphere annular modes (NAM and SAM), and the Pacific–North American (PNA) teleconnection pattern. For global warming scenarios, in contrast to most previous studies that show a large increase in AR length and width and therefore the occurrence frequency of AR conditions at a given location, this study shows only a modest increase in these quantities. However, the model produces a large increase in strong ARs with the frequency of category 3–5 ARs rising by roughly 100%–300% K^{-1}. The global mean AR intensity as well as AR intensity percentiles at most percent ranks increases by 5%–8% K^{-1}, roughly consistent with the Clausius–Clapeyron scaling of water vapor. Finally, the results point out the importance of AR IVT thresholds in quantifying modeled AR response to global warming.

KEYWORDS: Atmospheric circulation; Extratropical cyclones; Climate change; Water vapor; General circulation models; Model evaluation/performance

1. Introduction

Atmospheric rivers (ARs) are long, narrow, and transient corridors of strong horizontal water vapor transport typically associated with a low-level jet stream ahead of the cold front of an extratropical cyclone. They cover only a small fraction (~10%) of Earth's surface but account for ~90% of poleward water vapor transport outside of the tropics (Zhu and Newell 1998). ARs frequently lead to heavy precipitation where they are forced upward by ascent in the warm conveyor belt or by mountains over populated regions such as the west coasts of North and South America and western Europe (e.g., Ralph et al. 2004; Neiman et al. 2008; Lavers and Villarini 2015). Their impacts often extend eastward into the interior of the continents (e.g., Rutz et al. 2014; Lavers and Villarini 2013) and stretch as far as the polar ice caps as ARs transport large amounts of heat and moisture poleward, affecting the ice sheet's water mass and energy budgets (Gorodetskaya et al. 2014; Neff et al. 2014). ARs can profoundly impact local hydroclimates by generating floods (e.g., Ralph et al. 2006; Neiman et al. 2011; Lavers and Villarini 2013; Barth et al. 2017; Nayak and Villarini 2017) or alleviating drought (e.g., Dettinger 2013). Because ARs play such an important role in the global hydrological cycle, local water resources, regional weather and climate extremes, and other areas of societal importance (e.g., strong winds), it is imperative to understand and predict the AR phenomenon, especially their variations from subseasonal to interannual time scales as well as their change in future warmer climates (e.g., Payne et al. 2020).

Global climate models (GCMs) have until recently been utilized to study the AR phenomena and their response to global warming. Accurate climate projections of high-impact weather and climate extremes such as flood and drought would depend on the model's ability to simulate the observed AR climatology and variability in response to a large-scale environment. Most previous modeling studies of ARs focused on the west coasts of North America (e.g., Dettinger 2011; Gao et al. 2015; Hagos et al. 2016; Payne and Magnusdottir 2015; Pierce et al. 2013; Radić et al. 2015; Shields and Kiehl 2016a,b) and Europe (Gao et al. 2016; Lavers et al. 2013; Ramos et al. 2016; Shields and Kiehl 2016a) with Espinoza et al. (2018) being an exception, who investigated the AR response to warming over the entire globe despite using relatively coarse-resolution phase 5 of the Coupled Model Intercomparison Project (CMIP5) models. However, the ability/quality of coarse-resolution GCMs in representing ARs may be questionable due to their inability to resolve ARs' sharp horizontal gradient of vapor transport. Indeed, Guan and Waliser (2017) have pointed out considerable challenges for state-of-the-art weather/climate models in simulating the fundamental characteristics of ARs. In particular, they indicated the importance of the models' horizontal resolution to the overall quality of the AR simulations.

The goal of this study is to provide a systematic evaluation of the ability of the Geophysical Fluid Dynamics Laboratory's (GFDL's) new moderately high-resolution global climate model to simulate the observed AR characteristics and response to large-scale climate variability. Thereby, we also document the model that has been used for GFDL's participation in phase 6 of the Coupled Model Intercomparison

---

Corresponding author: Ming Zhao, ming.zhao@noaa.gov

DOI: 10.1175/JCLI-D-20-0241.1

Project (CMIP6; Eyring et al. 2016) and the High Resolution Model Intercomparison Project (HighResMIP; Haarsma et al. 2016). The rest of the paper is organized as follows. Section 2 describes the model, simulations, and the AR detection method. Section 3 provides an evaluation of the model simulated AR characteristics, climatology, and variability compared to the results from the ECMWF interim reanalysis (ERA-Interim, hereinafter ERA-I) product (Dee et al. 2011). Section 4 documents the model simulated AR response to global warming. Section 5 provides a summary.

2. The model, simulations, and AR detection method

The model we utilized for this study is a high-resolution version of the GFDL atmospheric model version 4 (AM4) documented in Zhao et al. (2018a,b). AM4 has been used in GFDL's new physical climate model CM4 (Held et al. 2019) and Earth system model ESM4 (Dunne et al. 2020) for GFDL's participation in CMIP6 (Eyring et al. 2016). In addition, AM4 has also been used in GFDL's Seamless System for Prediction and Earth System Research (SPEAR) documented in Delworth et al. (2020). AM4 employs a cubed-sphere topology for the atmospheric dynamical core. The default AM4 has 96 × 96 grid boxes per cube face (corresponding to a horizontal resolution of ~100 km). The version we used here has 192 × 192 grid boxes per cube face (thus referred to as C192AM4) corresponding to ~50-km horizontal grid spacing.

Due to the increase in horizontal resolution, we have modified the model's physics and dynamics time steps so that the C192AM4 has a gravity wave and Lagrangian dynamics step of 75 s, a vertical remapping and horizontal advection step of 600 s, and a physics and land model step of 1200 s. To increase the model's numerical stability, we use the fourth-order divergence damping (Zhao et al. 2012) instead of the sixth-order damping in AM4 (Zhao et al. 2018b). Furthermore, we have slightly tuned the model's cloud parameterization to increase the top-of-atmosphere (TOA) net downward radiative fluxes, which helps to reduce the cold bias in coupled model simulations of the historical sea surface air temperature (SST). In particular, the fall velocity of precipitating cloud ice has been slightly reduced with the tuning parameter c_1 (Zhao et al. 2018b) changed from 0.9 in AM4 to 0.8 in C192AM4. The cloud erosion time scales (Zhao et al. 2018b) are also reduced. The cloud tunings together amount to roughly 1 W m^{-2} increase in downward net TOA radiative flux in simulations with observed SSTs and sea ice concentrations. Other than this, we do not expect the cloud tunings to dramatically affect the model's simulation characteristics and we have verified that the present-day climatological bias patterns simulated by the C192AM4 are indeed very similar to that of AM4 (Zhao et al. 2018a) for all fields we have examined. As mentioned in section 1, the C192AM4 model has been used for GFDL's participation in the CMIP6 HighResMIP (Haarsma et al. 2016). The simulation data generated by this model will be shared by the broader CMIP6 community.

In this study, we focus on four C192AM4 simulations forced by prescribed SSTs, sea ice concentrations, radiative gases, and aerosol emissions. The first (below referred to as PRESENT) is a present-day simulation for the period of 1950–2014, with the model forced by the observed daily SSTs, sea ice concentrations, and radiative gases following the CMIP6 HighResMIP specifications. This simulation corresponds to the HighResMIP Tier 1 highresSST-present simulation (Haarsma et al. 2016). The second (below referred to as FUTURE) corresponds to the HighResMIP Tier 3 highresSST-future simulation covering the 2015–50 period. The future SSTs and sea ice concentrations were generated by the CMIP5 coupled model projections based on the representative concentration pathway 8.5 (RCP8.5) scenario (Haarsma et al. 2016). The specifications of the future radiative gases and aerosol emissions follow the CMIP6 Shared Socioeconomic Pathways 5 (SSP5), which contains emissions high enough to produce a radiative forcing of 8.5 W m^{-2} in 2100. In addition to the two simulations proposed by the CMIP6 HighResMIP, we have also conducted a pair of idealized simulations. The control simulation is a present-day climatological run (below referred to as CLIMO) with the model forced by monthly climatological SSTs and sea ice concentrations averaged over the 1980–2014 period and with radiation (solar and radiative gases) and aerosol emissions fixed at the year 2010 condition. Thus, the simulation does not contain interannual variability of forcing. The idealized global warming simulation is identical to CLIMO except with SSTs uniformly increased by 4 K (referred to as P4K below). The two warming simulations are utilized here to explore possible AR responses to future global warming.

There are a number of methods published in literature for detecting ARs on gridded model or reanalysis data. Shields et al. (2018) describe a recent project for comparing the different approaches. For this study, we use a recent one developed by Guan and Waliser (2015) that is particularly suitable for global AR analysis. This method uses high-frequency (6-hourly) output of zonal and meridional vertically integrated vapor transport (IVT) to compute the IVT magnitude at each grid cell. The algorithm starts with thresholding each instantaneous IVT field based on the 85th percentile specific to each season (i.e., percentile calculated over all time steps during the 5 months centered on that month) and grid cell with a fixed lower limit of 100 kg $\mathrm{m}^{-1}\,\mathrm{s}^{-1}$. Thus, the IVT threshold may be written in the form $\mathrm{IVT}_0(\text{month}, y, x)$ with each monthly point representing an overlapping 5-month season centered on that month. The identified AR candidates are then checked for the geometry requirement of length $>$ 2000 km, length-to-width ratio $>$ 2, and other considerations indicative of the AR conditions. They include a requirement of appreciable poleward transport of moisture ($>$50 kg $\mathrm{m}^{-1}\,\mathrm{s}^{-1}$) and coherence of IVT direction (i.e., more than half of the grid cells in an object must have their IVT directions within 45° from the object's mean IVT direction). The AR detection algorithm provides output of AR shape, axis, and landfall location as well as some basic measurement of each detected AR such as length, width, mean zonal and meridional IVT, and the coherence of IVT direction (Guan and Waliser 2015).

We use the ERA-I data at a horizontal resolution of 0.75° × 0.75° (lat × lon) for the period of 1979–2014. To facilitate model comparisons with the ERA-I results, the model output were first interpolated from its native cubed-sphere grid to a lat–lon grid at the same resolution as in ERA-I. We then use the identical AR detection method for both the model simulations and the ERA-I data and compare the AR statistics for the common period of 1979–2014. To analyze the AR responses to large-scale circulation patterns, we use monthly mean SST, sea level pressure, and 500-hPa geopotential height data to identify various large-scale circulation patterns such as El Niño–Southern Oscillation (ENSO), the Northern and Southern Hemisphere annular mode (NAM, SAM), and the Pacific–North American teleconnection pattern (PNA). Some of these analyses involve the use of empirical orthogonal function (EOF) analysis. The corresponding principal component (PC) time series are used to identify the positive and negative phases of a circulation pattern for compositing the anomalous AR frequencies.

3. Present-day AR characteristics and variability

We begin with a comparison of the probability density function (PDF) of some key AR parameters between the PRESENT simulation and the ERA-I results (see Fig. 1). The statistics are generated from roughly 6.2×10^5 AR objects identified from 6-hourly IVT maps for 36 years over the 1979–2014 period. Note the AR detection method does not track individual ARs over time so each IVT map is treated independently (Guan and Waliser 2015). Globally, there are on average 17 252 AR objects per year in PRESENT, which is roughly 3.9% more than that from the ERA-I (16 610 yr^{-1}). The average AR numbers detected from each IVT map are roughly 11.8 for PRESENT and 11.4 for ERA-I.

While both PRESENT and ERA-I produce a similar PDF of AR length-to-width ratio (r) with a peak at ~6.5, PRESENT tends to generate relatively more (fewer) ARs for $r > 9$ ($r < 9$) than the ERA-I (Fig. 1a). This is because PRESENT produces systematically narrower ARs in width (see Fig. 1c) but little difference in the AR length PDF compared to ERA-I. Figures 1d–f further show that PRESENT well reproduces the latitudinal distribution of the ARs' centroid location as well as their maximum equatorward and poleward extent compared to ERA-I.

PRESENT produces not only narrower but also stronger ARs than ERA-I as can be seen in Fig. 1g. In particular, PRESENT generates relatively more (less) ARs for IVT greater (less) than 440 $\mathrm{kg\,m^{-1}\,s^{-1}}$ compared to ERA-I. The median values of IVT for PRESENT and ERA-I are respectively 391 and 377 $\mathrm{kg\,m^{-1}\,s^{-1}}$. Figures 1h and 1i further show that PRESENT produces stronger ARs for both the zonal and meridional component of IVT. Since we used the coarse-grained model data at the same resolution as the ERA-I, the narrower and stronger ARs in PRESENT are likely due to the model's formulations in dynamical core and/or physics parameterizations (Zhao et al. 2018b) instead of its slightly higher horizontal resolution than ERA-I.

Figure 1j shows the PDF of the ARs' mean IVT direction, which is defined as the angle of the mean IVT vector measured in a clockwise direction from the north. Both PRESENT and ERA-I produce two peaks: one at ~65° and the other ~115°. The two peaks correspond to the Northern and Southern Hemisphere (NH and SH) ARs. The model tends to slightly underestimate the NH peak at ~65°. Figure 1k shows the same distribution as Fig. 1j except in polar coordinates. It is clear that the two peaks correspond to the eastward and poleward transport of water vapor in the two hemispheres. Finally, Fig. 1l shows the PDF of the coherence of AR IVT direction, which is defined as the fraction of the AR grid cells with their IVT directed within 45° of the AR's mean IVT direction. Both PRESENT and ERA-I produce a distribution peaking sharply at 1, suggesting that the vast majority of the detected ARs are spatially coherent in transporting water vapor. The coherence is rarely less than 0.8 for both PRESENT and ERA-I. Note the AR detection algorithm requires the coherence to be at least 0.5 to be a qualified AR candidate.

We compare in Fig. 2 the AR zonal scale defined as the fraction of zonal distance spanned by all ARs at a given latitude. PRESENT reproduces very well the ERA-I results with only small underestimation in the deep tropics where ARs are rare. In the NH (SH) middle latitudes both PRESENT and ERA-I exhibit a fractional zonal scale of ~8% (~11%), consistent with previous observational studies (e.g., Zhu and Newell 1998; Guan and Waliser 2015). Despite the small spatial coverage, ARs produce roughly 80%–90% of total meridional IVT in the midlatitudes of both hemispheres, which are also well simulated by PRESENT (Fig. 2, right legend/ordinate). Guan and Waliser (2017) showed the difficulties of the state-of-the-art weather/climate models in simulating the fractional total meridional IVT accounted for by ARs and cast doubt on the fidelity of the global water and energy cycles represented in the models they examined. The realistic simulations of the AR characteristic in PRESENT give us more confidence in using this model for studies of AR variability and future change as presented below.

Before we describe the modeled AR frequency variability, we first evaluate the modeled spatial distribution of climatological AR frequency computed as the fractional occurrence of AR conditions at a given location for the 1979–2014 period. Figure 3 compares the AR frequency between PRESENT and ERA-I for the November to March (NDJFM) and May to September (MJJAS) seasons with the bias patterns shown in Figs. 3c and 3f respectively. PRESENT well captures the AR frequency distribution with the pattern correlation coefficients exceeding 0.99 and root-mean-square (RMS) errors below 0.008 for both seasons. However, there are significant regional biases. For example, in the NDJFM season, PRESENT produces too many ARs in Alaska and northwestern Canada, but not enough along the West Coast of the United States. Over the North Atlantic and European sector, PRESENT tends to slightly underestimate (overestimate) the landfalling ARs in the United Kingdom (northwestern Africa and southwestern Europe). In the MJJAS season, the largest bias appears to be an underestimation over the southeast coast of Asia and an overestimation over the subtropical central Pacific. In addition, PRESENT also tends to produce too many ARs over the northwestern Canada and Alaska, but not enough ARs over most parts of North America.

We compare in Fig. 4 the seasonal anomalies of AR frequency between PRESENT and ERA-I. In the NDJFM season, ERA-I shows enhanced AR activities over the northeastern Pacific extending into the West Coast of the

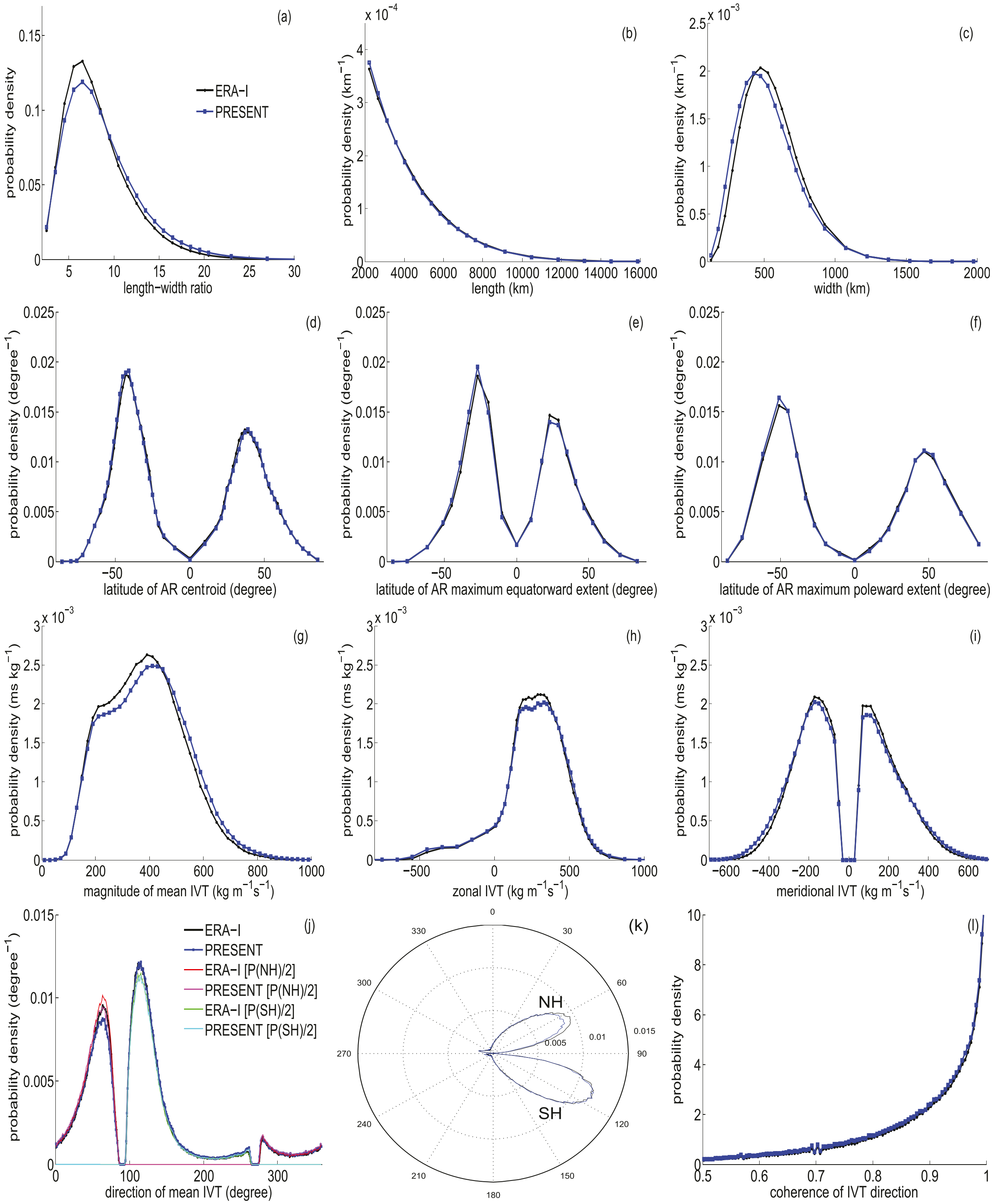

FIG. 1. A comparison of the ERA-I (black) and PRESENT (blue) simulated probability density functions for (a) AR length–width ratio, (b) AR length, (c) AR width, (d) AR centroid latitude, (e) latitude of AR maximum equatorward extent, (f) latitude of AR maximum poleward extent, (g) AR mean IVT magnitude, (h) AR mean zonal IVT, (i) AR mean meridional IVT, (j) AR mean IVT direction, and (l) the coherence of AR IVT direction (see text for the definition). The PDF (divided by 2) of AR mean IVT direction for NH (red and magenta) and SH (green and cyan) ARs are also plotted in (j) for comparison. (k) As in (j), except plotted in polar coordinates (only the PDFs of global ARs plotted for clarity) with azimuth representing the direction of mean IVT and radial distance the probability density. The two lobes correspond to the NH and SH ARs as indicated by the legend.

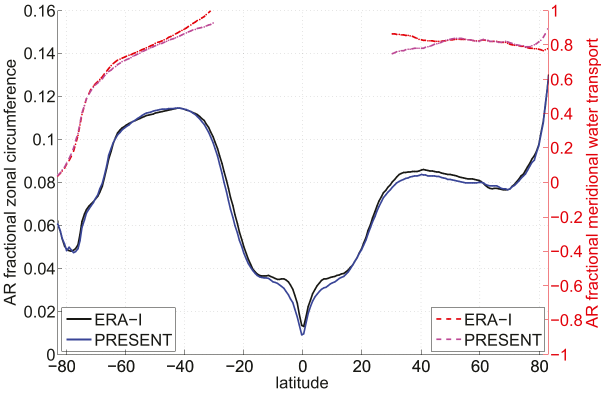

FIG. 2. A comparison of AR fractional zonal scale and meridional water transport between ERA-I and PRESENT. The AR fractional zonal scale (black and blue lines; left legend/ordinate) is defined as the total zonal distance spanned by all ARs at a given latitude divided by the zonal circumference at that latitude. The AR fractional meridional water transport (red and magenta lines; right legend/ordinate) is defined as the fraction of total meridional water transport due to all ARs at a given latitude.

United States, the subtropical North Atlantic extending toward the west coast of Europe, the Middle East, and the western Mediterranean Sea and nearby northern Africa. These are all well captured by PRESENT although the model tends to slightly underestimate (overestimate) the magnitude of the anomalies over the Pacific (Atlantic) sector. In the MJJAS season, ERA-I displays enhanced AR activities over the southeastern Pacific extending toward Chile, the west coast of Australia, and South Africa. These are also well captured by PRESENT. Overall the pattern correlation coefficient for the anomalous AR frequency between PRESENT and ERA-I is 0.96 with the model's global RMS error below 0.005 for both seasons (see Figs. 4c,f). The bias patterns exhibit some similarities to their corresponding seasonal climatological bias patterns shown in Figs. 3c and 3f.

Previous studies show that AR frequency is modulated by various large-scale modes of climate variability such as ENSO, NAM/SAM, and PNA. Thus, it would be important to evaluate to what extent PRESENT can reproduce the observed present-day AR frequency variability. Figure 5 shows the difference in AR frequency between the El Niño and La Niña conditions for both the NDJFM and MJJAS seasons. El Niño and La Niña conditions are selected here based on a threshold of ±0.8°C for the Oceanic Niño Index (ONI), computed as 3-month running mean of the ERSST.v4 (Extended Reconstructed Sea Surface Temperature version 4; Huang et al. 2015) SST anomalies for the Niño-3.4 region (5°N–5°S, 120°–170°W). During El Niño conditions, ERA-I exhibits enhanced AR activities in the NDJFM season over a number of subtropical and extratropical regions including the west coast of North America, the Gulf of Mexico extending into the subtropical North Atlantic toward the west coast of Europe, the east coast of Asia, the Middle East, the south Indian Ocean, the South Pacific convergence zone (SPCZ), and part of the South Atlantic. These anomalous increases in AR frequency are broadly captured by PRESENT with a pattern correlation coefficient of 0.68 and RMS error of 0.017. It is interesting to note there is some interhemispheric symmetry in the pattern of AR frequency response to ENSO in both PRESENT and ERA-I during the NDJFM season. However, the model also displays significant regional biases. For example, the increase in AR frequency over the northeastern Atlantic does not extend farther north into the United Kingdom, which would negatively affect the modeled U.K. landfalling ARs. Similarly, in the North Pacific sector, the model tends to underestimate the increase in AR frequency over the west coast of Canada. For the MJJAS season, the pattern correlation is slightly lower (0.65) with a significantly larger RMS error (0.023), which may be due to the fact that the ENSO signal and their effects tend to peak at boreal winter. Nevertheless, PRESENT appears to capture reasonably well the increase in AR frequency in the southeastern Pacific, which is important to the landfalling ARs in central Chile.

The NAM (SAM) is a major large-scale mode of atmospheric circulation characterized by sea level pressure anomalies of one sign in the Arctic (or Antarctic) region, balanced by anomalies of the opposite sign in the surrounding extratropical regions. When the NAM (SAM) is in its positive phase, a ring of strong winds circulating around the North (South) Pole confines colder air across polar regions. This belt of winds becomes weaker and more distorted in the negative phase of the NAM (SAM), which allows an easier equatorward penetration of colder, Arctic (Antarctic) air masses and increased storminess into the midlatitudes. To explore the effects of NAM (SAM) on ARs, we constructed the NAM (SAM) index by EOF analysis of the monthly mean sea level pressure (SLP) anomalies poleward of 20°N (20°S) for both ERA-I and PRESENT. Because the NAM patterns can be significantly different between the NH summer and winter, we conduct EOF analysis of NAM patterns separately for the NDJFM and MJJAS seasons. The positive (negative) phase of NAM for each season are then selected based on a positive (negative) threshold of 0.8 standard deviation of the PC time series for the first EOF of the corresponding season. Since the SAM pattern does not change much across the seasons, we simply conduct the EOF analysis using all monthly SLP anomalies and then select the positive (negative) phase of SAM based on a positive (negative) threshold of 0.8 standard deviation of the PC time series for the first EOF.

We compare in Fig. 6 the difference in AR frequency between the positive and negative phase of NAM (NH maps) and SAM (SH maps) for both the NDJFM and MJJAS seasons. In the NDJFM season, during the positive phase of NAM, ERA-I exhibits a large increase in AR frequency from the coast of the Baja California Peninsula stretching northeastward across the continental United States and the Atlantic into the northern Europe. Meanwhile, there is a large reduction in AR frequency to the south from the Gulf of Mexico extending northeastward across the subtropical North Atlantic into southern Europe. In addition, there is also a large reduction of ARs over the Labrador Sea and southwestern Greenland. In the Pacific sector, the increase in AR frequency tends to be more zonal, centered around 50°N with a band of reductions at the south centered around 30°N. A similar pattern of anomalous AR

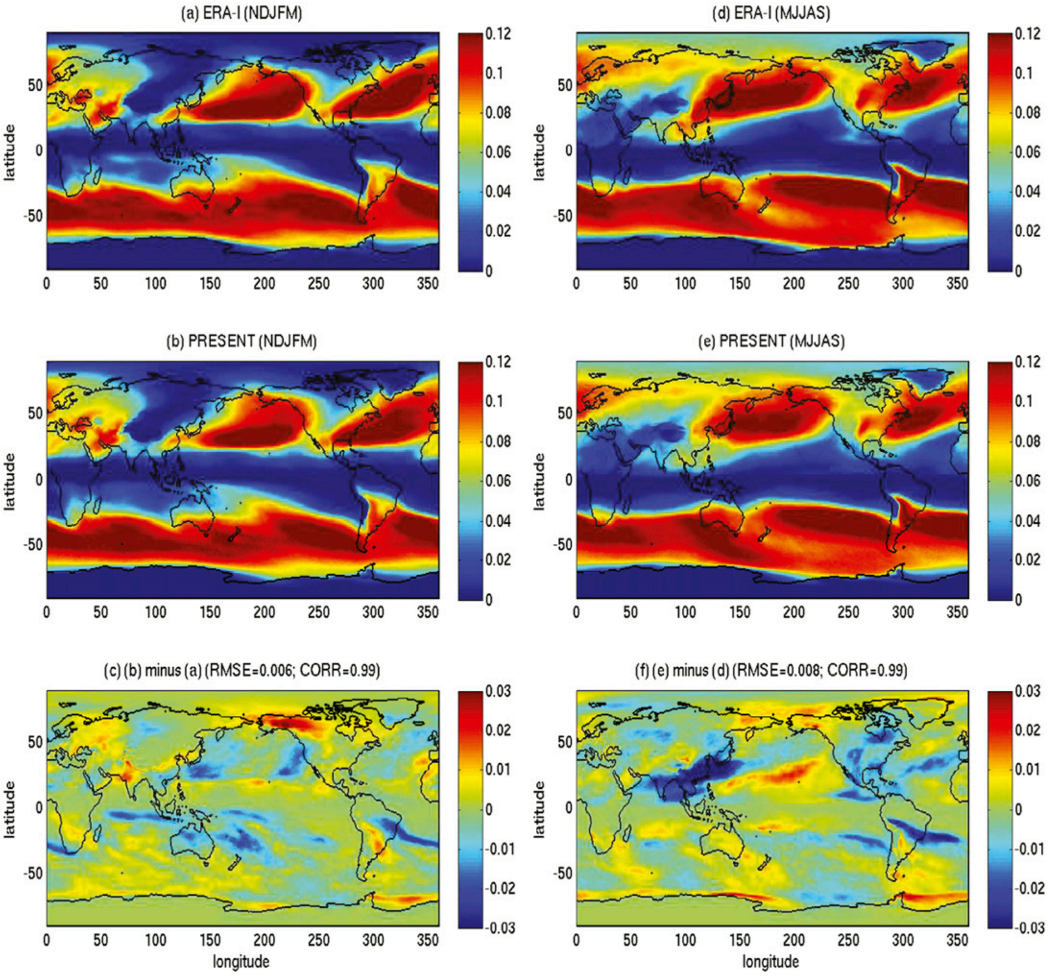

FIG. 3. (left) Geographical distribution of climatological (1979–2014) AR frequency (computed as fractional occurrence of AR conditions at a given location from all IVT maps analyzed; unit: fraction of time steps) from (a) ERA-I and (b) PRESENT for the November–March season (NDJFM). (c) Results of (b) minus (a) with the global pattern correlation coefficient and RMS error shown above the panel. (right) As in the left column, but for the May–September (MJJAS) season.

frequency can also be seen in the MJJAS season despite a significantly weaker magnitude, especially in the North Pacific. The response of AR frequency to NAM is well captured by PRESENT although the model tends to slightly underestimate the anomalies over the North Atlantic sector and overestimate them over the North Pacific sector (see Fig. 6, NH). Overall, the pattern correlation for the NH is, respectively, 0.86 and 0.75 for the NDJFM and MJJAS season with a RMS error of 0.017 and 0.016.

The SH maps in Fig. 6 show the AR frequency response to SAM. During the positive phase of SAM, ERA-I shows broadly a poleward shift of AR frequency, which is also well captured by PRESENT. The pattern correlation for the SH is respectively 0.85 and 0.83 for the NDJFM and MJJAS season with a RMS error of 0.018 and 0.015. In general, the shift of AR frequency in both NH and SH is consistent with the poleward migration of storm tracks during the positive phase of NAM and SAM. Combining the AR response to NAM in the NH and to SAM in the SH, the global pattern correlation coefficient of the anomalous AR frequency between PRESENT and ERA-I is 0.86 (0.79) for the NDJFM (MJJAS) season with a RMS error of 0.018 (0.015).

Finally, we examine the impact of the PNA teleconnection pattern on AR frequency. The PNA pattern is one of the most prominent modes of low-frequency variability in the NH extratropics, which is characterized by a wave train signal that spans from the equatorial Pacific through the northwest of North America to the southeastern part of North America. The positive phase of the PNA pattern features above-average heights in the vicinity of Hawaii and over the intermountain region of North America, and below-average heights located south of the Aleutian Islands and over the southeastern United States. The PNA pattern is associated with strong fluctuations in the strength and location of the East Asian jet stream. The

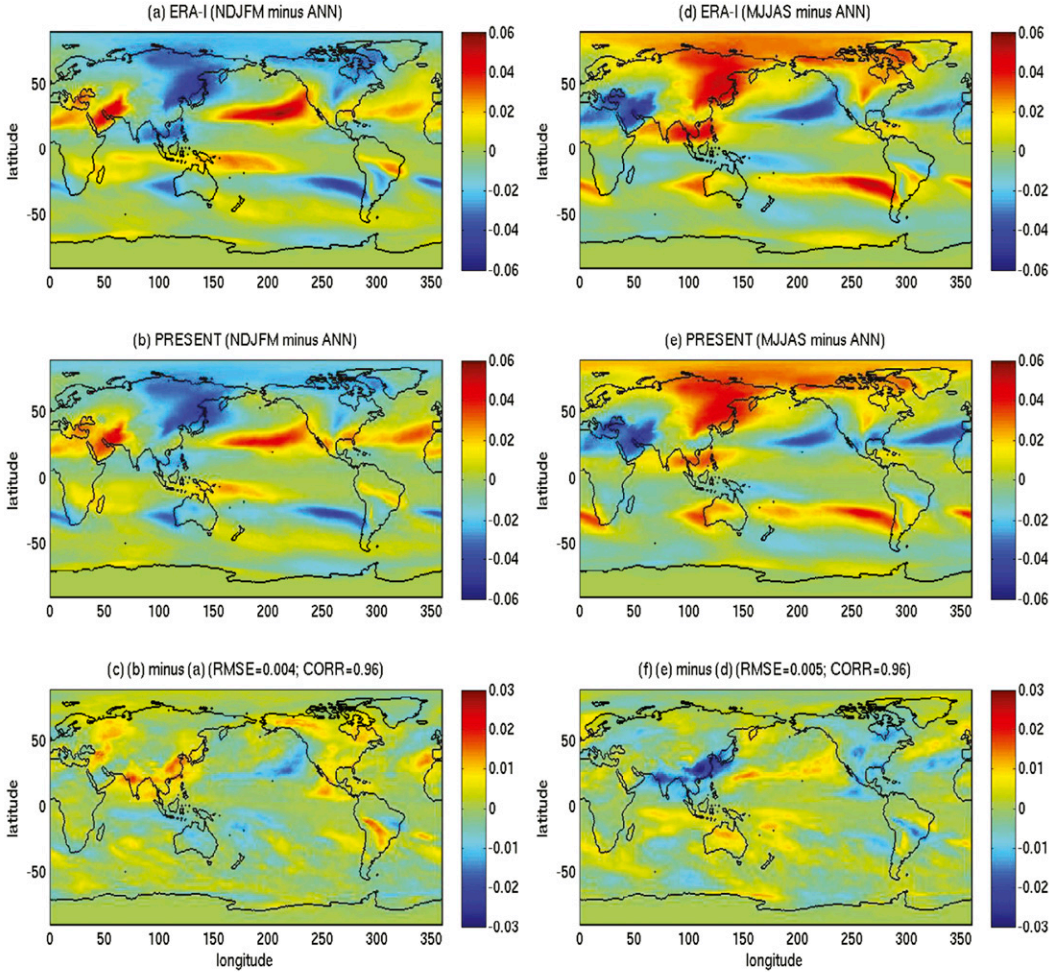

FIG. 4. (left) The anomalous AR frequency averaged over the 1979–2014 period from (a) ERA-I and (b) PRESENT for NDJFM. (c) Results of (b) minus (a) with the global pattern correlation coefficient and RMS error shown above the panel. (right) As in the left column, but for MJJAS.

positive phase is associated with an enhanced East Asian jet stream and with an eastward shift in the jet exit region toward the western United States. The negative phase is associated with a westward retraction of the jet stream toward eastern Asia, blocking activity over the high latitudes of the North Pacific, and a strong split-flow configuration over the central North Pacific. Although the PNA pattern is a natural internal mode of climate variability, it is also strongly affected by ENSO. The positive (negative) phase of the PNA pattern tends to be associated with the Pacific warm El Niño (cold La Niña) episodes.

To explore the effects of PNA on AR frequency, we constructed the PNA index by EOF analysis of the monthly anomalies of 500-hPa geopotential height for all months from 1979 to 2014 over the NH region of 0°–90°N, 120°–360°E. The positive (negative) phase of PNA is selected based on a positive (negative) threshold of 0.8 standard deviations of the PC time series for the second EOF. Figure 7 shows the difference in AR frequency between the positive and negative phase of PNA for both the NDJFM and MJJAS seasons. In the NDJFM season, during the positive phase of PNA, ERA-I shows an increased AR frequency from the middle latitudes of North Pacific to the northwest coast of the United States and the west coast of Canada extending into the interior regions of Canada. Meanwhile, there is a large reduction of AR frequency centered around the Bering Sea. In the subtropical northeastern Pacific, there is a reduction of AR activities that extends northeastward across the Baja California Peninsula and the southern United States. In the Atlantic sector, the ERA-I displays a broad northward shift of AR activities in response to the positive PNA, which is somewhat similar to the AR response to positive NAM. The pattern of AR frequency variability associated with the PNA is broadly captured by PRESENT despite significant regional biases such as an underestimation of the AR increase in the middle latitudes of North Pacific and an overestimation of the AR reduction in Alaska and the nearby Bering Sea in response to the positive PNA. The overall NH pattern correlation is 0.81 in the NDJFM

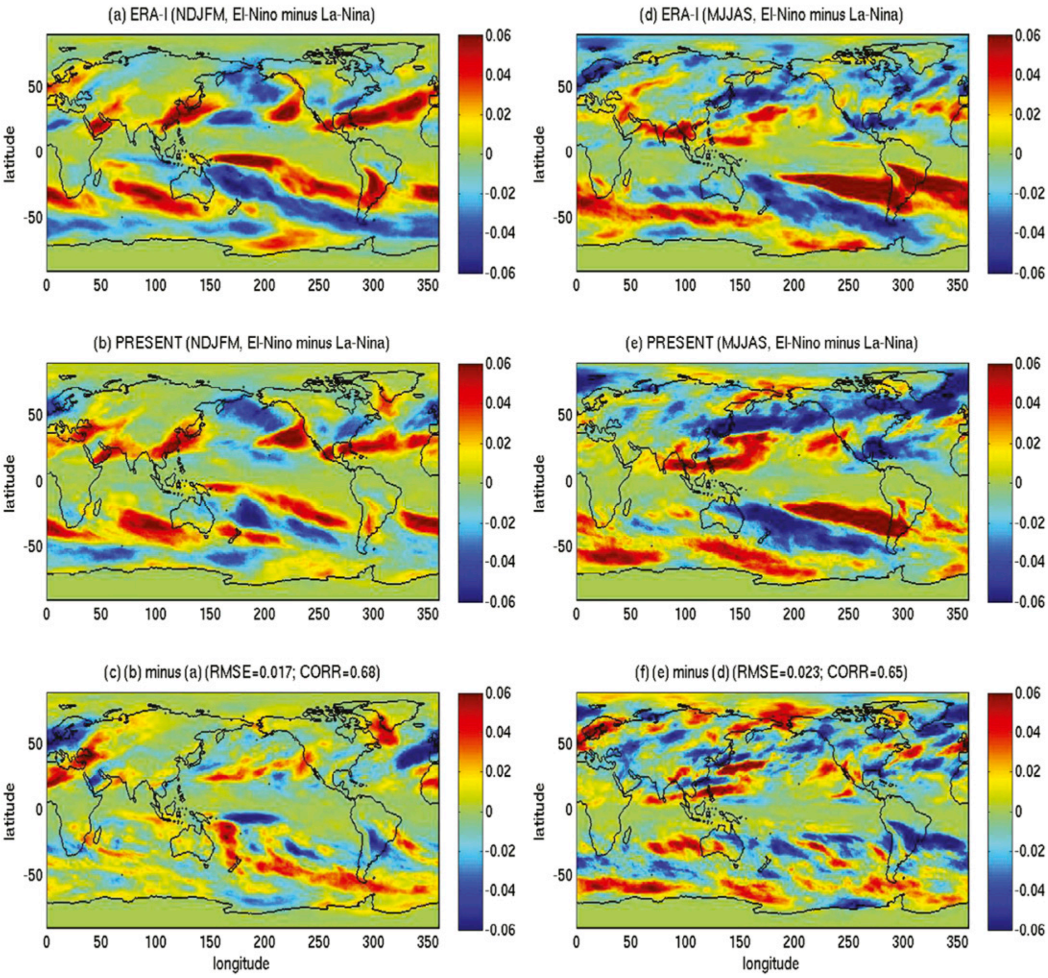

FIG. 5. (left) The difference in NDJFM AR frequency between El Niño and La Niña conditions from (a) ERA-I and (b) PRESENT. (c) Results of (b) minus (a) with the global pattern correlation coefficient and RMS error shown above the panel. (right) As in the left column, but for MJJAS.

season with a RMS error of 0.015. The pattern correlation is significantly lower (0.66) in the MJJAS season with a larger RMS error (0.027), consistent with generally weaker effects of the PNA in boreal summer.

4. AR response to global warming

The realistic simulations of the present-day AR characteristics and frequency variability motivate our further investigation of the AR response to future global warming. As described in section 2, we have conducted two global warming simulations (i.e., FUTURE and P4K) with prescribed SSTs and sea ice conditions. FUTURE may be considered as a more realistic warming scenario since it includes the future SSTs and sea ice concentrations projected from the CMIP5 coupled models as well as specifications of future time-varying radiative gases and aerosol emissions. In contrast, P4K is an idealized global warming experiment in which we only increase SSTs uniformly by 4 K. P4K allows us to study the effects of global mean SST warming in isolation from other factors such as the interannual variations of forcings and the detailed SST warming patterns, which are quite uncertain in future projections. Figure 8 shows the spatial distribution of the surface air temperature warming anomalies from the two pairs of global warming simulations. Note that both panels have been normalized by their corresponding global mean warming (0.99 K for FUTURE minus PRESENT; 4.53 K for P4K minus CLIMO) so that we can focus on their differences in warming pattern. While both simulations tend to produce more warming over land, FUTURE contains much larger polar warming amplifications over the high-latitude sea ice covering regions. Compared to P4K, FUTURE has less relative warming in the eastern portion of the North and South Pacific, the broad Southern Ocean, the northern North Atlantic, and Antarctica.

We apply the same AR detection method used in PRESENT for the three additional simulations (FUTURE, CLIMO, and P4K) except that for a given simulation, we use the IVT 85th percentile of its own simulation for thresholding its IVT fields.

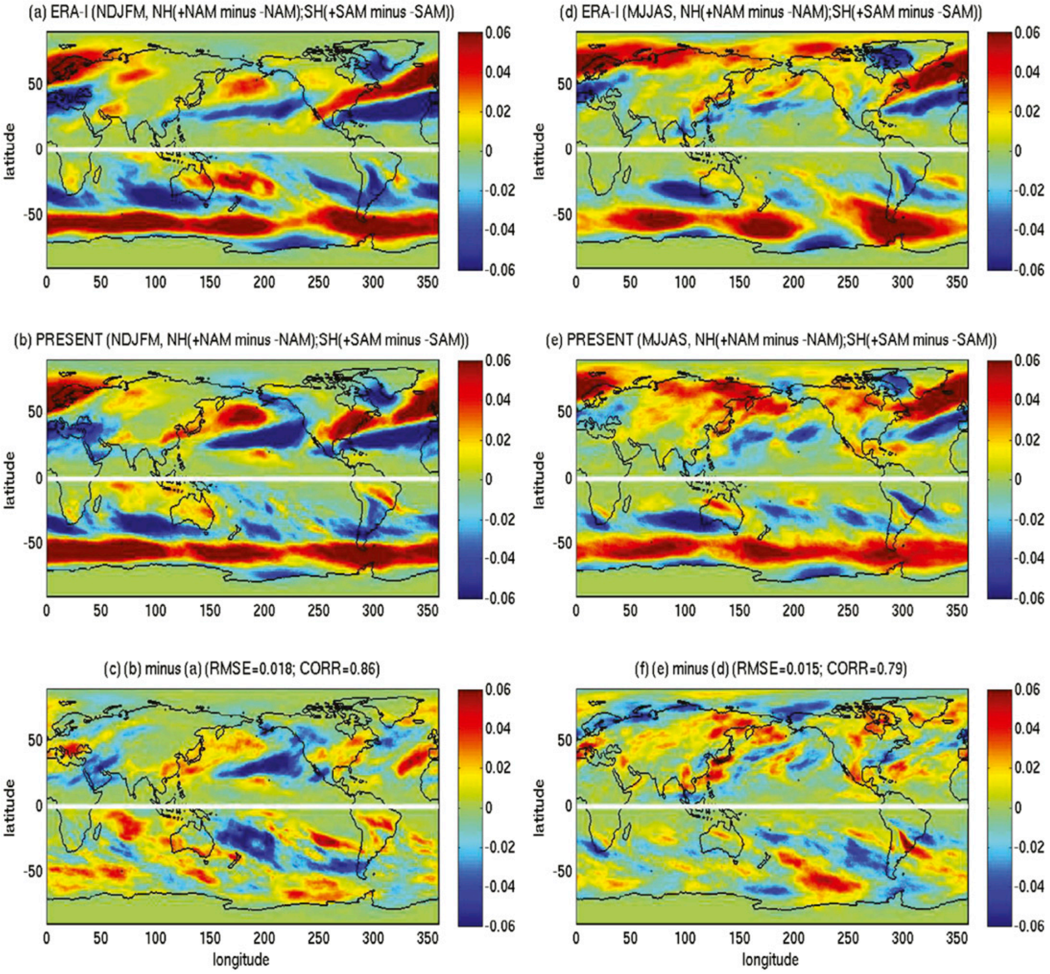

FIG. 6. (left) The difference in NDJFM AR frequency between the positive and negative phases of NAM (NH) and SAM (SH) from (a) ERA-I and (b) PRESENT. (c) Results of (b) minus (a) with the global pattern correlation coefficient and RMS error shown above the panel. (right) As in the left column, but for MJJAS.

This would automatically and consistently take into account the change in background state of moisture transport in the global warming experiments. We refer to this choice of IVT thresholds as our standard choice. However, in literature, most global warming studies of ARs used the IVT thresholds based on their present-day or historical simulations. For example, Espinoza et al. (2018) used the IVT 85th percentile derived from their historical simulations for detecting ARs in their future simulations. To explore the consequence of this different choice of IVT thresholds, we have also conducted the AR detection for FUTURE and P4K using the IVT thresholds identical to their corresponding control simulation. These results are referred to as FUTURE-CTLIVT0 and P4K-CTLIVT0 respectively.

Table 1 shows the global and annual number of AR objects from each simulation (or analysis). The model produces very small changes in the global number of ARs in response to warming with P4K-CTLIVT0 being an exception, which exhibits roughly 4.7% K^{-1} reduction. For the roughly 2-K (4-K) global mean warming by the end of twenty-first century as projected by the CMIP5 multimodel mean under the RCP4.5 (RCP8.5) scenario, this would indicate roughly a 9.4% (18.8%) reduction of global AR numbers. This is roughly consistent with Espinoza et al. (2018), who report ~10% fewer ARs globally in future (2073–96) warmer climate simulated in CMIP5 models. However, the reduction in global numbers of ARs in P4K-CTLIVT0 disappears nearly completely when we use the IVT 85th percentile of its own simulation (i.e., P4K) as the IVT thresholds for AR detection.

To understand the effect of different choices in AR IVT thresholds on the simulated AR response to global warming, Fig. 9 shows the NDJFM season 85th percentile of IVT magnitude derived from each simulation. While the increase from PRESENT to FUTURE is relatively small, it is huge from CLIMO to P4K due to its factor of 4.6 increase in surface air temperature. If we use the IVT 85th percentile from CLIMO for P4K, this would lead to a large increase in the size of AR candidates. The increase in an AR candidate's size can result

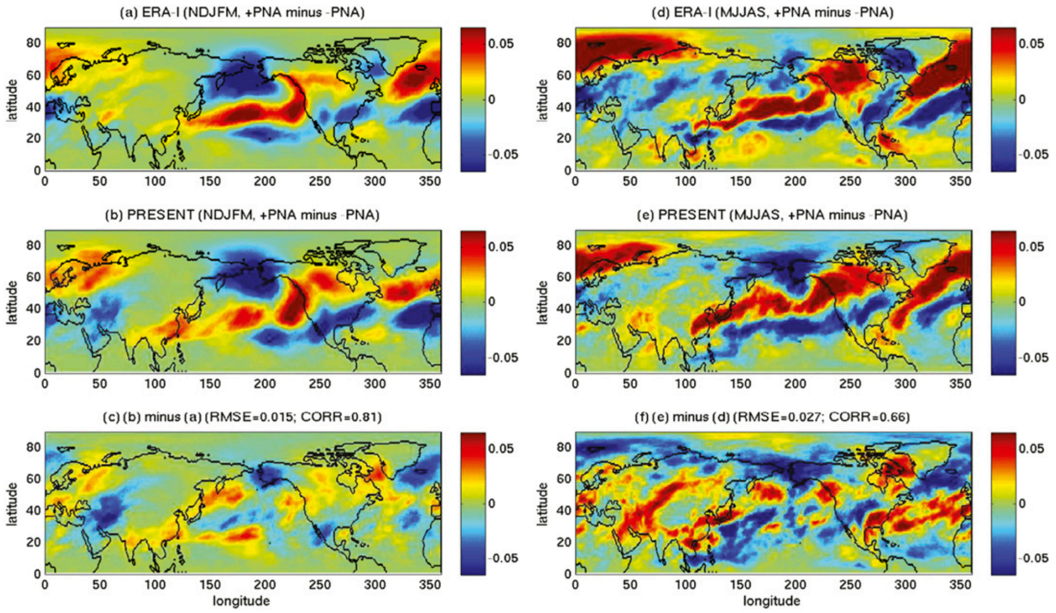

FIG. 7. (left) The difference in NDJFM AR frequency between positive and negative phases of the PNA from (a) ERA-I and (b) PRESENT. (c) Results of (b) minus (a) with the pattern correlation coefficient and RMS error shown above the panel. (right) As in the left column, but for MJJAS.

in a reduction of total number of ARs because 1) it may aggregate multiple ARs into an AR complex and 2) the enlarged size may lead to its failure of satisfying other AR criteria such as the requirement for IVT coherence, direction, and geometry. It is also possible that the reduced IVT thresholds may lead to additional ARs identified, but these effects appear to be less important.

To give an example, Figs. 10a and 10b compare a snapshot of the ARs detected based on an instantaneous IVT field from P4K using the two different IVT thresholds. The two ARs (see Fig. 10a) identified in the South Pacific and South Atlantic Ocean using our standard IVT thresholds are combined into a huge one (see Fig. 10b) spanning across the two ocean basins if we use the IVT 85th percentile from CLIMO as the thresholds. Although the combined one exhibits a structure that does not resemble a typical AR shape, it still passes all of the AR criteria and survives as a modeled AR. It is however possible that an enlarged AR candidate no longer satisfies the AR requirement and is subsequently rejected as an AR. For example, Figs. 10a and 10b show that one AR near southern Australia and three other ARs near southern Africa identified using our standard AR thresholds disappear if we use the CLIMO IVT thresholds. This is due to the increased candidate sizes (see Figs. 10c,d) that result in their failure of satisfying other AR criteria. Both of the misidentifications would artificially reduce the number of AR objects and this becomes more severe as the magnitude of global mean warming increases. Indeed, we find the problem occurs quite frequently in P4K-CLIMOIVT0. This is the primary reason we do not use the IVT 85th percentile from the present-day control simulations for detecting ARs in the future warming experiments. Below we will focus on the AR response using our standard choice of IVT threshold but we also include FUTURE-CTLIVT0 and P4K-CTLIVT0 for comparisons with earlier results in literature.

We now present in Fig. 11a the AR intensity PDF from two pairs of global warming simulations. As expected, CLIMO produces an intensity PDF very similar to PRESENT except with a slightly stronger peak at ~400 kg m^{-1} s^{-1}. This suggests a slight reduction of AR intensity variability in the climatological simulation with no interannual variability of SSTs and sea ice. Compared to their control simulations, both FUTURE and P4K exhibit a shift toward a higher intensity PDF. By contrast, P4K produces a much larger shift due primarily to its factor of 4.6 increase in global mean surface warming. When normalized to per 1 K of global mean warming, Fig. 11a (right legend/ordinate) shows that the two warming simulations produce a similar broad reduction of ARs at intensities below 450–500 kg m^{-1} s^{-1} and an increase at higher intensities. The mean AR IVT increases by 4.9% and 7.5% K^{-1} for FUTURE and P4K respectively. The model produces much larger percent increases in strong ARs with IVT greater than 800 kg m^{-1} s^{-1}. To put the changes in the context of a recent AR scale classification based on their potential hydrological impacts (Ralph et al. 2019), we include in Fig. 11a the possible range of AR scales at each IVT (see the colored horizontal bars). Based on this classification, our simulations suggest a roughly 100%–300% K^{-1} increase in category 3–5 ARs despite a slight reduction in the global number of ARs with warming. However, the AR intensity PDFs in FUTURE-CTLIVT0 and P4K-CTLIVT0 remain nearly unchanged except at very high intensities.

One issue with quantifying percent change in the frequency of an extreme event such as very strong ARs is that the probability of the event in present-day simulations is very low

(a) FUTURE minus PRESENT

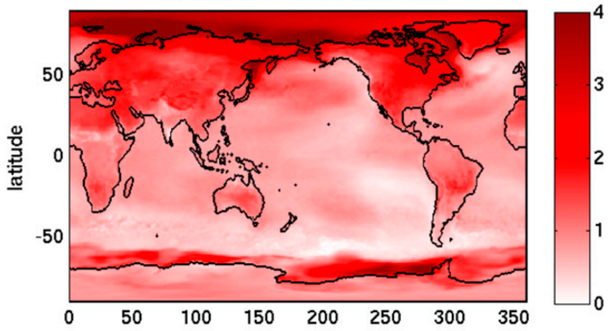

(b) P4K minus CLIMO

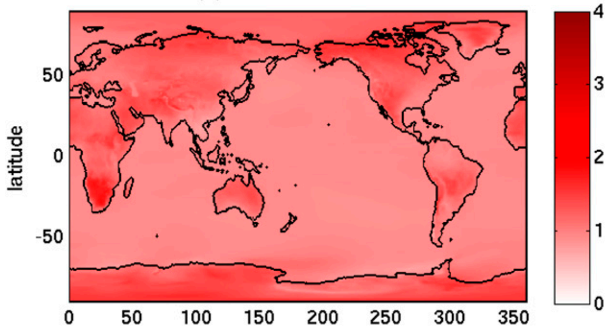

FIG. 8. Difference in annual mean surface air temperature between (a) FUTURE (2015–50 average) and PRESENT (1979–2014 average) and (b) P4K and CLIMO. Both (a) and (b) are normalized by their corresponding global mean warming (0.99 K for FUTURE minus PRESENT; 4.53 K for P4K minus CLIMO) so that their global mean warming are 1 K.

(approaching zero). A small increase in its frequency in warmer climates may lead to very large percent increases. To provide additional information on the changes of AR intensity, Fig. 11b further shows the percentile values of the modeled AR mean IVT magnitude and their response to warming. While FUTURE-CTLIVT0 and P4K-CTLIVT0 consistently show little changes except at the lower and higher end of the percent ranks, FUTURE and P4K display a large increase in all percentile values, indicating a systematic increase in AR intensity with warming across all intensity ranges. The magnitude of increase is ~5% and ~7.5% K^{-1} for FUTURE and P4K respectively, roughly consistent with the Clausius–Clapeyron scaling of water vapor (e.g., Held and Soden 2006).

A recent study suggests large increases (~25%) of AR length and width with warming in the CMIP5 models (Espinoza et al. 2018). To compare with this earlier study, we examine the change of the PDF for AR length and width from our simulations in Figs. 12a and 12b. Although there is a general shift of the AR length and width PDF toward larger values, the mean AR length and width increase only modestly (~1% K^{-1} or less) in FUTURE and P4K. In contrast, FUTURE-CTLIVT0 and P4K-CTLIVT0 show a much larger shift in the PDFs with the mean AR length/width increasing by ~5% and ~8% K^{-1}, respectively. These numbers would suggest a roughly 20%–30% increase in AR length/width for a global mean warming of ~4 K projected by the end of the twenty-first century under the RCP8.5 scenario. Thus, the FUTURE-CTLIVT0 and P4K-CTLIVT0 results are consistent with Espinoza et al. (2018), who used the IVT 85th percentile from historical simulations as the IVT thresholds for detecting ARs in future warming simulations. However, our results suggest that the magnitude of the increase in AR length/width depends strongly on the IVT thresholds used in warming simulations. This can be further seen in Figs. 12c and 12d, which show the percentile values for AR length/width and their response to warming. While FUTURE and P4K exhibit only a modest increase (1%–2% K^{-1}) in all percentiles of AR length/width, FUTURE-CTLIVT0 and P4K-CTLIVT0 generate a much larger increase (~5%–10% K^{-1}) due to their use of IVT thresholds from the control simulations. The response of AR length and width with warming is directly relevant to the occurrence frequency of AR conditions at any given locations as we present below.

We show in Figs. 13a and 13b the geographical distribution of the absolute and relative changes in annual AR frequency between FUTURE and PRESENT. The global area-weighted average of AR frequency increases by 1.4% K^{-1}, and this is consistent with the small increase in AR length and width in Fig. 12. Note that this change in global AR frequency is different from the change in global number of the AR objects, which actually exhibits a slight reduction as mentioned before. Regionally, the increase in AR frequency tends to occur over most parts of the middle and high latitudes including the Arctic Ocean, Greenland, northern North America, the Tibetan Plateau, and the Southern Ocean sea ice–covering regions. AR

TABLE 1. Global and annual number of AR objects identified from 6-hourly IVT maps and its percentage change with global warming.

Simulation and analysis	No. of AR objects (yr^{-1})	Percentage change (% K^{-1})
PRESENT	17 252	—
FUTURE	17 191	−0.36
FUTURE-CTLIVT0	17 212	−0.23
CLIMO	17 370	—
P4K	17 359	−0.01
P4K-CTLIVT0	13 677	−4.7

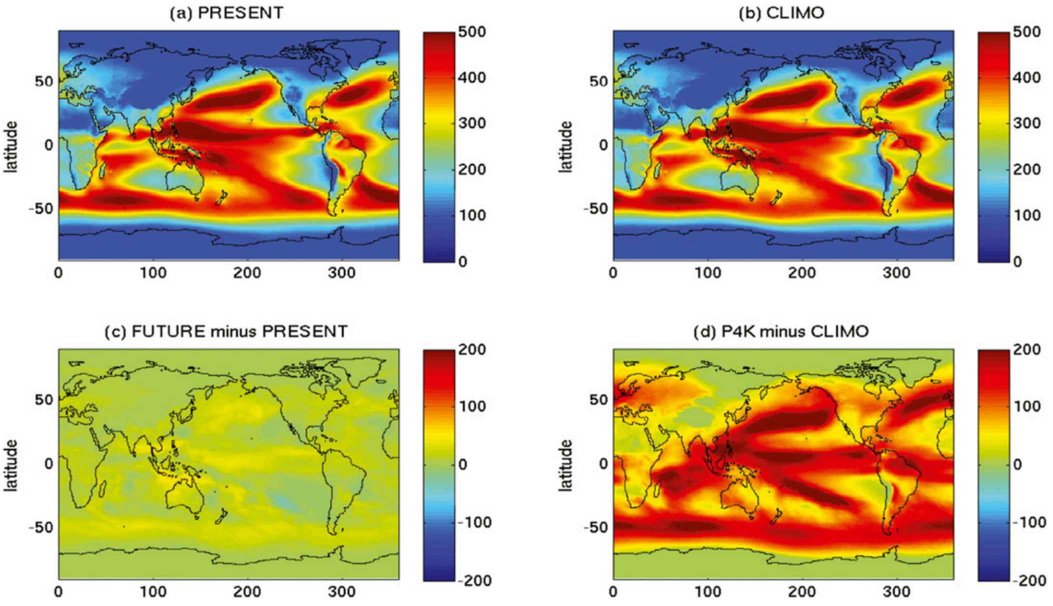

FIG. 9. (a) The NDJFM 85th percentile of IVT magnitude (values below 100 are set to 100 following the algorithm) derived from PRESENT and used for its AR detection (kg m^{-1} s^{-1}). (b) As in (a), but for CLIMO. (c) As in (a), but showing the difference between FUTURE and PRESENT. (d) As in (c), but for the difference between P4K and CLIMO.

frequency tends to decrease over most parts of the tropical and subtropical oceans. Large percentage changes tend to occur over the regions of climatologically fewer AR conditions such as the polar sea ice–covering regions and the Tibetan Plateau.

Figures 13c and 13d display plots similar to Figs. 13a and 13b except for the change in AR frequency between P4K and CLIMO. Compared to FUTURE, the response is spatially much smoother due presumably to the lack of interannual

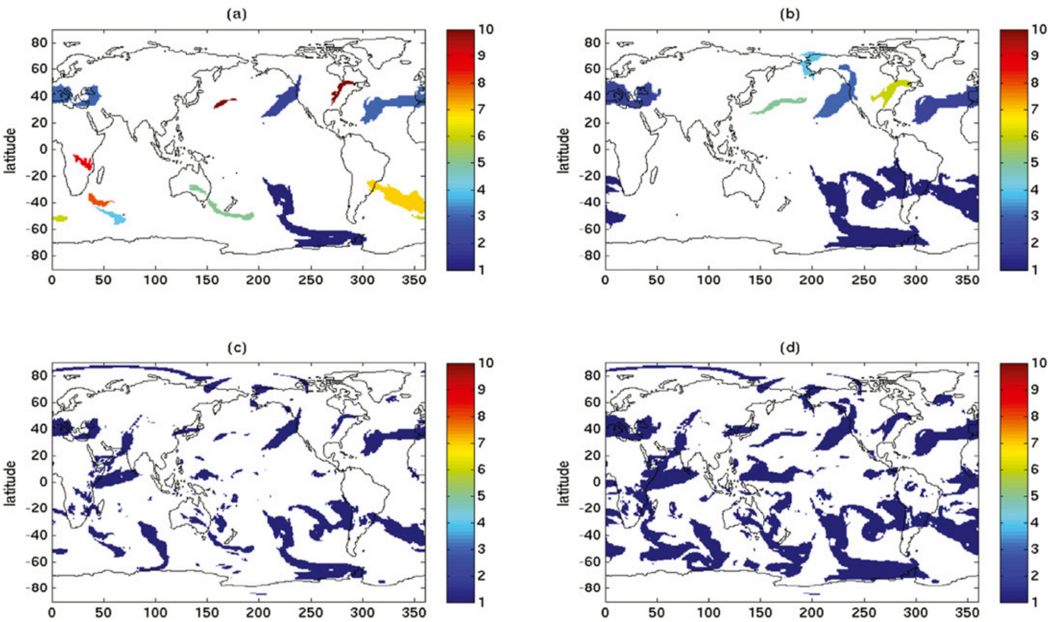

FIG. 10. (a) A snapshot of ARs detected based on an instantaneous IVT field from P4K using the IVT 85th percentile derived from P4K as the IVT thresholds (i.e., our standard IVT threshold). The detected ARs are color coded. (b) As in (a), except using the IVT 85th percentile from CLIMO as the IVT thresholds (i.e., an alternative IVT thresholds used in previous studies) (c) Regions where the IVT magnitude is greater than the IVT 85th percentile from P4K and a fixed lower limit of 100 kg m^{-1} s^{-1}. These regions are used for detecting the ARs in (a). (d) Regions where the IVT magnitude is greater than the IVT 85th percentile from CLIMO and a fixed lower limit of 100 kg m^{-1} s^{-1}. These regions are used for detecting the ARs in (b).

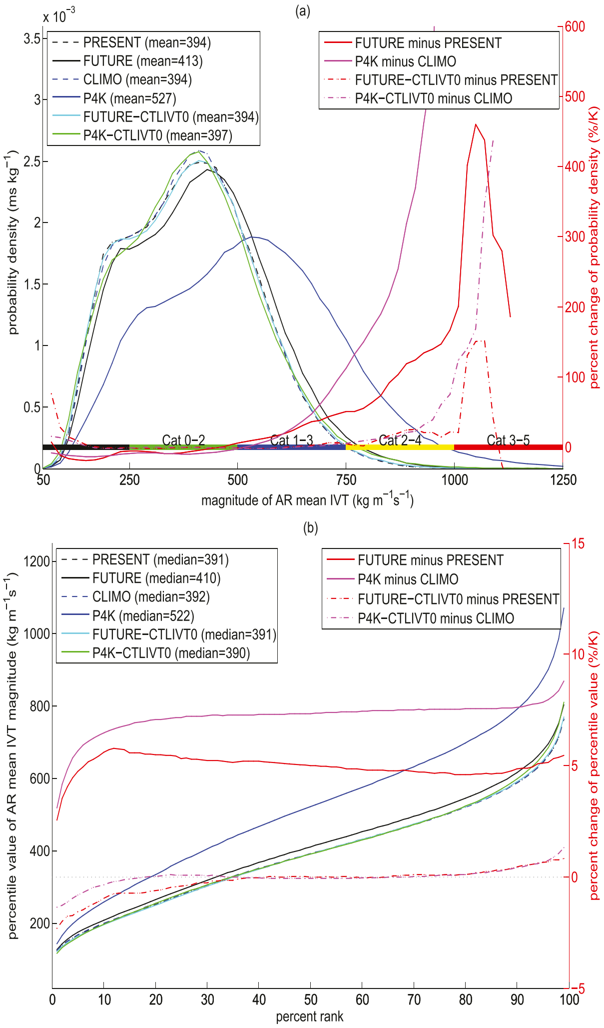

FIG. 11. (a) Probability density function (left legend/ordinate) of the magnitude of AR mean IVT from two pairs of the warming simulations. FUTURE-CTLIVT0 and P4K-CTLIVT0 are the same as FUTURE and P4K, respectively, except with the IVT thresholds replaced by their corresponding control simulations (see text for details). Red and magenta lines (right legend/ordinate) show the percentage change of the probability density (i.e., the absolute difference divided by the control value at each bin and multiplied by 100) normalized to 1 K of global mean warming (i.e., divided by the global mean value of warming) between each warming simulation and its control. The colored horizontal bars indicate possible range of AR intensity following the classification by Ralph et al. (2019), which takes into account both AR IVT magnitudes and AR durations. (b) As in (a), except showing the percentile values of AR mean IVT magnitude (left legend/ordinate) and their percentage change per 1 K of global mean warming (right legend/ordinate).

variability and uniform SST warming. Nevertheless, there are some broad similarities between the two warming experiments such as the increase in AR frequencies over the northern and southern high latitudes, and the reduction or little change in the tropics. However, there are also significant differences between the two. In particular, the uniform warming tends to produce a distinct increase in AR frequency over the West Coast of the United States and the subtropical central North Pacific near the southern edge of the North Pacific maximum climatological AR frequency (see Fig. 3). In addition, P4K produces an elongated band of increase in AR frequency originating from the SPCZ and extending all the way into the central Chile. The significant differences in regional changes of AR frequency between the two warming scenarios suggests both the importance of SST warming patterns and that the effects of global mean warming may be masked by transient SST warming patterns in the near-term predictions of ARs. Despite the regional differences, the global averaged increase (1.9% K^{-1}) in AR frequency between P4K and CLIMO is only slightly larger than that (1.4% K^{-1}) from FUTURE and PRESENT.

Finally, we show in Fig. 14 that the AR frequency increases drastically with warming if we replace the IVT thresholds used in FUTURE and P4K by their corresponding control simulations (i.e., PRESENT and CLIMO). The global mean increase is 11% and 12% K^{-1} for FUTURE-CTLIVT0 and P4K-CTLIVT0, respectively. Regionally, the increase in many of the middle and high latitudes regions are more than 20% K^{-1}. Given the ~4 K global mean surface warming projected at the end of twenty-first century under the RCP8.5 scenario, this would suggest ~44%–48% increase in global mean AR frequency and ~80% increase in AR frequency in many of the northern and southern high latitudes. While the FUTURE-CTLIVT0 and P4K-CTLIVT0 results are generally consistent with Espinoza et al. (2018), our analysis suggests that the results depend strongly on the IVT thresholds used in warming simulations. In particular, we argue that the use of IVT 85th percentile from historical or present-day control simulations may not be appropriate for future warming simulations, especially when the magnitude of global mean warming is large as we have discussed in Figs. 9 and 10.

5. Summary

We have described a moderately high-resolution (50 km) version of the GFDL AM4 (i.e., C192AM4) used in simulations of present-day climatology, variability, and future changes in AR statistics. The identical model has been used for GFDL's participation in CMIP6 HighResMIP. This C192AM4 forced by the historical SSTs, sea ice concentrations, radiative gases, and aerosol emissions well captures many aspects of the observed AR characteristics compared to ERA-I results. They include the PDF of AR length, width, length-to-width ratio, geographical location, and the magnitude and direction of AR mean IVT. The model typically generates narrower and stronger ARs than the ERA-I and this is likely due to the model's formulation of dynamical core and physics parameterizations (Zhao et al. 2018b). The C192AM4 also reproduces well the observed climatological distribution of AR frequency despite significant regional biases. These biases include an overestimation of AR activities in Alaska and northwestern

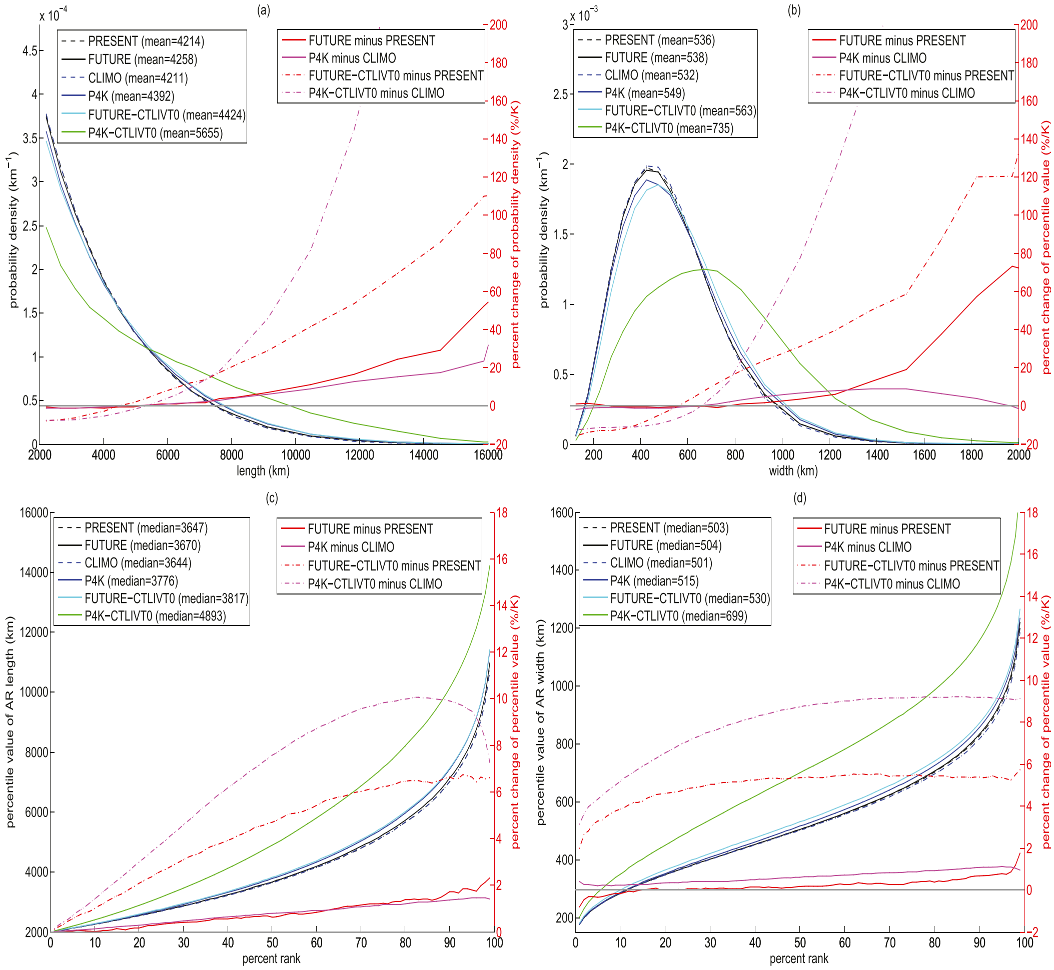

FIG. 12. (top) As in Fig. 11a, but for (a) AR length and (b) AR width. (bottom) As in Fig. 11b, but for (c) AR length and (d) AR width.

Canada and an underestimation along the West Coast of the United States.

To provide a critical evaluation of the model's ability in simulating AR frequency variability to large-scale environments, we composite the anomalous AR frequency between the positive and negative phases of several major modes of climate variability including the ENSO, the NAM/SAM, and the PNA pattern for both the model and ERA-I. Our results suggest that the model can reasonably well reproduce the observed AR frequency variability with a pattern correlation coefficient of 0.68 for ENSO, 0.86 for NAM/SAM, and 0.81 for PNA during the NH winter (NDJFM). The pattern correlation coefficients are slightly lower during the NH summer (MJJAS) due probably to the fact that these modes of variability and their effects tend to peak during the NH winter.

The realistic simulations of present-day AR characteristics and variability motivate our further investigation of the AR response to future global warming. In contrast to previous studies that suggest large increases in AR length and width and therefore the occurrence frequency of AR conditions at a given location, our study suggests only a modest increase in these quantities. Despite this, the model produces a large increase in strong ARs with the frequency of category 3–5 ARs rising by roughly 100%–300% K^{-1}. The global mean AR intensity as well as the AR intensity percentiles at most percent ranks (10%–99%) increases by 5%–8% K^{-1}, roughly consistent with the Clausius–Clapeyron scaling of water vapor. Our results also suggest significant uncertainties in predicting regional changes in AR frequency. Some of the effects of global mean warming on regional changes in AR frequency may be masked by the transient SST warming patterns in near-term AR predictions.

Finally, our analysis points out that the modeled AR response to global warming depends strongly on the IVT thresholds used in warming simulations. The large difference in the changes of AR length/width/frequency with warming between the present study and some earlier studies (e.g., Espinoza et al. 2018) is due primarily to the difference in the IVT thresholds used in future warming simulations. In particular, we argue that the use of IVT 85th percentile from the

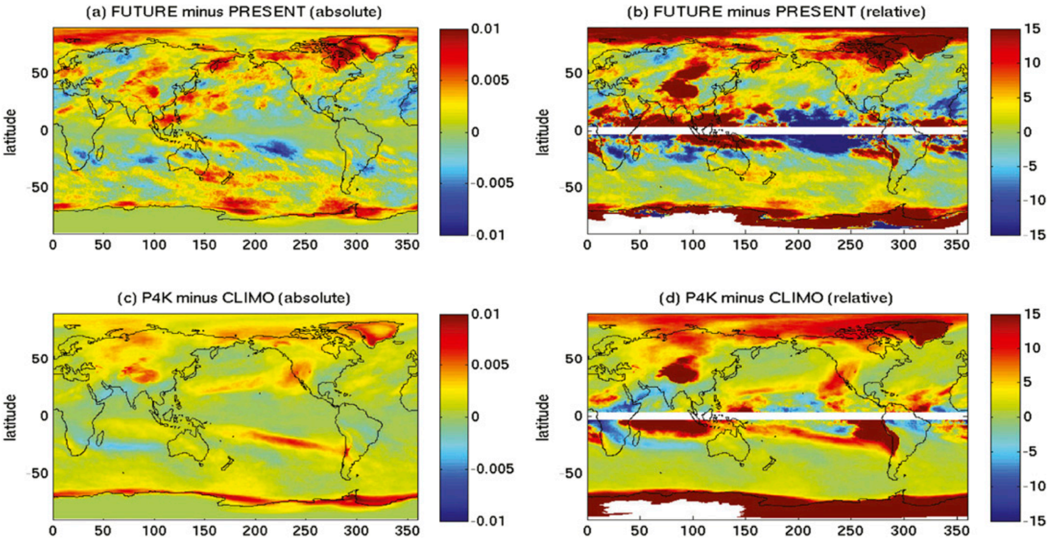

FIG. 13. (a) Geographical distribution of the absolute changes in annual AR frequency between FUTURE and PRESENT normalized by the global mean surface warming (unit: fraction of time steps per 1 K of global mean warming; K^{-1}). (b) As in (a), but for the relative changes defined as the absolute changes divided by the AR frequency from the control simulation at each location and multiplied by 100 (% K^{-1}). The equatorial (2.5°S–2.5°N) region is masked out due to its very small AR frequency in control simulations. (c) As in (a), but for P4K and CLIMO. (d) As in (b), but for P4K and CLIMO.

present-day or historical simulations may not be appropriate for future warming simulations especially when the magnitude of warming is large. It would lead to a significant overestimation of the increase in AR length/width and frequency of occurrence and an underestimation of the increase in AR intensity with warming. This would have important implications for AR-associated hazards as the climate warms.

Acknowledgments. We provide the model code at http://data1.gfdl.noaa.gov/nomads/forms/am4.0/. The C192AM4 simulation data can be obtained from https://esgf-node.llnl.gov/search/cmip6/. We acknowledge the World Climate Research Programme CMIP6 HIRESMIP Working Group for providing forcing data and some of the simulation setup, and the Earth System Grid Federation (ESGF) for archiving the data and providing access, and the multiple funding agencies who support CMIP6 and ESGF. We thank Bin Guan for providing the AR detection code and Alex Chang for some initial analysis of ARs. We are grateful for helpful comments and suggestions from Leo Donner, Steve Garner, Tom Knutson, and Michael A. Zhao.

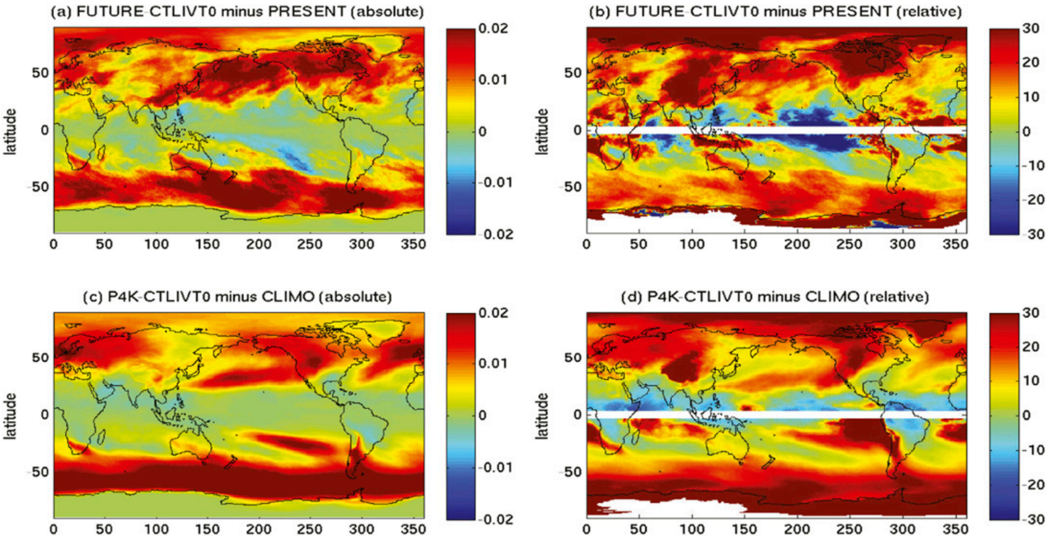

FIG. 14. As in Fig. 13, except the AR detection in warming simulations uses the same IVT thresholds as those used in their corresponding control simulations. Note the scales of the color bars are different from those in Fig. 13.

REFERENCES

Barth, N. A., G. Villarini, M. A. Nayak, and K. White, 2017: Mixed populations and annual flood frequency estimates in the western United States: The role of atmospheric rivers. *Water Resour. Res.*, **53**, 257–269, https://doi.org/10.1002/2016WR019064.

Dee, D. P., and Coauthors, 2011: The ERA-Interim reanalysis: Configuration and performance of the data assimilation system. *Quart. J. Roy. Meteor. Soc.*, **137**, 553–597, https://doi.org/10.1002/qj.828.

Delworth, T. L., and Coauthors, 2020: SPEAR: The next generation GFDL modeling system for seasonal to multidecadal prediction and projection. *J. Adv. Model. Earth Syst.*, **12**, e2019MS001895, https://doi.org/10.1029/2019MS001895.

Dettinger, M. D., 2011: Climate change, atmospheric rivers, and floods in California—A multimodel analysis of storm frequency and magnitude changes. *J. Amer. Water Resour. Assoc.*, **47**, 514–523, https://doi.org/10.1111/j.1752-1688.2011.00546.x.

——, 2013: Atmospheric rivers as drought busters on the U.S. West Coast. *J. Hydrometeor.*, **14**, 1721–1732, https://doi.org/10.1175/JHM-D-13-02.1.

Dunne, J. P., and Coauthors, 2020: The GFDL Earth System Model version 4.1 (GFDL-ESM4.1): Overall coupled model description and simulation characteristics. *J. Adv. Model. Earth Syst.*, https://doi.org/10.1029/2019MS002015, in press.

Espinoza, V., D. E. Waliser, B. Guan, D. A. Lavers, and F. M. Ralph, 2018: Global analysis of climate change projection effects on atmospheric rivers. *Geophys. Res. Lett.*, **45**, 4299–4308, https://doi.org/10.1029/2017GL076968.

Eyring, V., S. Bony, G. Meehl, C. A. Senior, B. Stevens, R. Stouffer, and K. E. Taylor, 2016: Overview of the Coupled Model Intercomparison Project Phase 6 (CMIP6) experimental design and organization. *Geosci. Model Dev.*, **9**, 1937–1958, https://doi.org/10.5194/gmd-9-1937-2016.

Gao, Y., J. Lu, L. R. Leung, Q. Yang, S. Hagos, and Y. Qian, 2015: Dynamical and thermodynamical modulations on future changes of landfalling atmospheric rivers over western North America. *Geophys. Res. Lett.*, **42**, 7179–7186, https://doi.org/10.1002/2015GL065435.

——, ——, and ——, 2016: Uncertainties in projecting future changes in atmospheric rivers and their impacts on heavy precipitation over Europe. *J. Climate*, **29**, 6711–6726, https://doi.org/10.1175/JCLI-D-16-0088.1.

Gorodetskaya, I. V., M. Tsukernik, K. Claes, M. F. Ralph, W. D. Neff, and N. P. M. V. Lipzig, 2014: The role of atmospheric rivers in anomalous snow accumulation in East Antarctica. *Geophys. Res. Lett.*, **41**, 6199–6206, https://doi.org/10.1002/2014GL060881.

Guan, B., and D. E. Waliser, 2015: Detection of atmospheric rivers: Evaluation and application of an algorithm for global studies. *J. Geophys. Res. Atmos.*, **120**, 12 514–12 535, https://doi.org/10.1002/2015JD024257.

——, and ——, 2017: Atmospheric rivers in 20 year weather and climate simulations: A multimodel, global evaluation. *J. Geophys. Res. Atmos.*, **122**, 5556–5581, https://doi.org/10.1002/2016JD026174.

Haarsma, R. J., and Coauthors, 2016: High Resolution Model Intercomparison Project (HighResMIP v1.0) for CMIP6. *Geosci. Model Dev.*, **9**, 4185–4208, https://doi.org/10.5194/gmd-9-4185-2016.

Hagos, S., L. R. Leung, J.-H. Yoon, J. Lu, and Y. Gao, 2016: A projection of changes in landfalling atmospheric river frequency and extreme precipitation over western North America from the large ensemble CESM simulations. *Geophys. Res. Lett.*, **43**, 1357–1363, https://doi.org/10.1002/2015GL067392.

Held, I. M., and B. J. Soden, 2006: Robust responses of the hydrological cycle to global warming. *J. Climate*, **19**, 5686–5699, https://doi.org/10.1175/JCLI3990.1.

——, and Coauthors, 2019: Structure and performance of GFDL's CM4.0 climate model. *J. Adv. Model. Earth Syst.*, **11**, 3691–3727, https://doi.org/10.1029/2019MS001829.

Huang, B., and Coauthors, 2015: Extended Reconstructed Sea Surface Temperature version 4 (ERSST.v4). Part I: Upgrades and intercomparisons. *J. Climate*, **28**, 911–930, https://doi.org/10.1175/JCLI-D-14-00006.1.

Lavers, D. A., and G. Villarini, 2013: The nexus between atmospheric rivers and extreme precipitation across Europe. *Geophys. Res. Lett.*, **40**, 3259–3264, https://doi.org/10.1002/grl.50636.

——, and ——, 2015: The contribution of atmospheric rivers to precipitation in Europe and the United States. *J. Hydrol.*, **522**, 382–390, https://doi.org/10.1016/j.jhydrol.2014.12.010.

——, R. P. Allan, G. Villarini, B. Lloyd-Hughes, D. J. Brayshaw, and A. J. Wade, 2013: Future changes in atmospheric rivers and their implications for winter flooding in Britain. *Environ. Res. Lett.*, **8**, 034010, https://doi.org/10.1088/1748-9326/8/3/034010.

Nayak, M. A., and G. Villarini, 2017: A long-term perspective of the hydroclimatological impacts of atmospheric rivers over the central United States. *Water Resour. Res.*, **53**, 1144–1166, https://doi.org/10.1002/2016WR019033.

Neff, W., G. P. Compo, F. M. Ralph, and M. D. Shupe, 2014: Continental heat anomalies and the extreme melting of the Greenland ice surface in 2012 and 1889. *J. Geophys. Res. Atmos.*, **119**, 6520–6536, https://doi.org/10.1002/2014JD021470.

Neiman, P. J., F. M. Ralph, G. A. Wick, Y. Kuo, T. Wee, Z. Ma, G. H. Taylor, and M. D. Dettinger, 2008: Diagnosis of an intense atmospheric river impacting the Pacific Northwest: Storm summary and offshore vertical structure observed with COSMIC satellite retrievals. *Mon. Wea. Rev.*, **136**, 4398–4420, https://doi.org/10.1175/2008MWR2550.1.

——, L. J. Schick, F. M. Ralph, M. Hughes, and G. A. Wick, 2011: Flooding in western Washington: The connection to atmospheric rivers. *J. Hydrometeor.*, **12**, 1337–1358, https://doi.org/10.1175/2011JHM1358.1.

Payne, A. E., and G. Magnusdottir, 2015: An evaluation of atmospheric rivers over the North Pacific in CMIP5 and their response to warming under RCP 8.5. *J. Geophys. Res. Atmos.*, **120**, 11 173–11 190, https://doi.org/10.1002/2015JD023586.

——, and Coauthors, 2020: Responses and impacts of atmospheric rivers to climate change. *Nat. Rev. Earth Environ.*, **1**, 143–157, https://doi.org/10.1038/s43017-020-0030-5.

Pierce, D. W., and Coauthors, 2013: The key role of heavy precipitation events in climate model disagreements of future annual precipitation changes in California. *J. Climate*, **26**, 5879–5896, https://doi.org/10.1175/JCLI-D-12-00766.1.

Radić, V., A. J. Cannon, B. Menounos, and N. Gi, 2015: Future changes in autumn atmospheric river events in British Columbia, Canada, as projected by CMIP5 global climate models. *J. Geophys. Res. Atmos.*, **120**, 9279–9302, https://doi.org/10.1002/2015JD023279.

Ralph, F. M., P. J. Neiman, and G. A. Wick, 2004: Satellite and CALJET aircraft observations of atmospheric rivers over the eastern North Pacific Ocean during the winter of 1997/98. *Mon. Wea. Rev.*, **132**, 1721–1745, https://doi.org/10.1175/1520-0493(2004)132<1721:SACAOO>2.0.CO;2.

——, ——, ——, S. I. Gutman, M. D. Dettinger, D. R. Cayan, and A. B. White, 2006: Flooding on California's Russian River: Role of atmospheric rivers. *Geophys. Res. Lett.*, **33**, L13801, https://doi.org/10.1029/2006GL026689.

——, J. J. Rutz, J. M. Cordeira, M. Dettinger, M. Anderson, D. Reynolds, L. J. Schick, and C. Smallcomb, 2019: A scale to characterize the strength and impacts of atmospheric rivers. *Bull. Amer. Meteor. Soc.*, **100**, 269–289, https://doi.org/10.1175/BAMS-D-18-0023.1.

Ramos, A. M., R. Tome, R. M. Trigo, M. L. R. Liberato, and J. G. Pinto, 2016: Projected changes in atmospheric rivers affecting Europe in CMIP5 models. *Geophys. Res. Lett.*, **43**, 9315–9323, https://doi.org/10.1002/2016GL070634.

Rutz, J. J., W. J. Steenburgh, and F. M. Ralph, 2014: Climatological characteristics of atmospheric rivers and their inland penetration over the western United States. *Mon. Wea. Rev.*, **142**, 905–921, https://doi.org/10.1175/MWR-D-13-00168.1.

Shields, C. A., and J. T. Kiehl, 2016a: Atmospheric river landfall-latitude changes in future climate simulations. *Geophys. Res. Lett.*, **43**, 8775–8782, https://doi.org/10.1002/2016GL070470.

——, and ——, 2016b: Simulating the Pineapple Express in the half degree Community Climate System Model, CCSM4. *Geophys. Res. Lett.*, **43**, 7767–7773, https://doi.org/10.1002/2016GL069476.

——, and Coauthors, 2018: Atmospheric River Tracking Method Intercomparison Project (ARTMIP): Project goals and experimental design. *Geosci. Model Dev.*, **11**, 2455–2474, https://doi.org/10.5194/gmd-11-2455-2018.

Zhao, M., I. M. Held, and S.-J. Lin, 2012: Some counterintuitive dependencies of tropical cyclone frequency on parameters in a GCM. *J. Atmos. Sci.*, **69**, 2272–2283, https://doi.org/10.1175/JAS-D-11-0238.1.

——, and Coauthors, 2018a: The GFDL global atmosphere and land model AM4.0/LM4.0: 1. Simulation characteristics with prescribed SSTs. *J. Adv. Model. Earth Syst.*, **10**, 691–734, https://doi.org/10.1002/2017MS001208.

——, and Coauthors, 2018b: The GFDL global atmosphere and land model AM4.0/LM4.0: 2. Model description, sensitivity studies, and tuning strategies. *J. Adv. Model. Earth Syst.*, **10**, 735–769, https://doi.org/10.1002/2017MS001209.

Zhu, Y., and R. E. Newell, 1998: A proposed algorithm for moisture fluxes from atmospheric rivers. *Mon. Wea. Rev.*, **126**, 725–735, https://doi.org/10.1175/1520-0493(1998)126<0725:APAFMF>2.0.CO;2.